Photoacoustics 34 (2023) 100567

Contents lists available at ScienceDirect

Photoacoustics

journal homepage: www.elsevier.com/locate/pacs

Research article

Tomographic reconstruction of picosecond acoustic strain pulses using automated angle-scan probing with visible light

Motonobu Tomoda [a,*], Hiroyuki Matsuo [a], Osamu Matsuda [a], Roberto Li Voti [b], Oliver B. Wright [c,d]

[a] Faculty of Engineering, Hokkaido University, Sapporo, 060-8628, Japan
[b] Department SBAI, Sapienza University of Roma, Via A. Scarpa 14, Roma, I-00161, Italy
[c] Hokkaido University, Sapporo, 060-0808, Japan
[d] Graduate School of Engineering, Osaka University, Yamadaoka 2-1, Suita, Osaka, 565-0871, Japan

ARTICLE INFO

Keywords:
Picosecond ultrasonics
Acoustic tomography
Brillouin scattering
Angle scan
Inverse problem
Singular value decomposition

ABSTRACT

By means of an ultrafast optical technique, picosecond acoustic strain pulses in a transparent medium are tomographically visualized at GHz frequencies. The strain distribution in BK7 glass is reconstructed from time-domain reflectivity changes of 415-nm probe light as a function of the optical incidence angle with 1 ps temporal and 120 nm spatial resolutions, enabled by automated angle scanning. The latter resolution is achieved owing to the commensurate acoustic wavelength. Applications include imaging strain, carrier and temperature distributions on ultrashort timescales.

1. Introduction

Imaging of ultrasonic wave propagation in the interior of materials is useful for probing structures therein. In general, photoelastic methods [1–5] for solid materials and Schlieren methods [1,6–16] or shadowgraphy [8,11,17–19] for liquids and gases can be used for ultrasonic field imaging. These are often combined with stroboscopic methods or high-speed video camera detection to make a time-resolved movie. However, GHz ultrasonic frequencies, corresponding to submicron wavelengths, cannot be investigated with these types of detection. Picosecond laser ultrasonics, which makes use of acoustic waves in the frequency range 10–1000 GHz, provides new opportunities to investigate internal structures or physical properties of thin films, microstructures or nanostructures [20,21]. In the conventional setup, ultrashort pump light pulses generate GHz longitudinal strain pulses in thin opaque films, and delayed probe light pulses detect the strain pulses that return to the surface after reflection at some internal inhomogeneity. To understand the strain propagation, analytical theory or numerical simulations have been used. However, no existing experimental method had been able to visualize picosecond ultrasonic pulses continuously during their propagation inside media. We previously developed an ultrafast tomographic optical technique that allows picosecond strain pulses to be profiled during propagation with infrared probe light in a homogenous and isotropic transparent medium through the photoelastic effect, by use of different probe angles of incidence at 830-nm wavelength [22]. We extend this approach to shorter optical wavelength probing at 415 nm with automated angle scanning, allowing for a spatial resolution ~120 nm, i.e., ~30% of the incident probe wavelength. This enhancement is facilitated by the smaller acoustic wavelength compared to the optical wavelength, enabling us to resolve GHz ultrasonic strain propagation in glass with roughly twice the spatial resolution previously attainable using this method.

2. Principle of the tomographic strain profiling technique

2.1. Outline of the technique

Consider the optical-incidence geometry of Fig. 1(a). The sample takes the form of a transparent hemisphere with an opaque film deposited on its flat surface to act as an optoacoustic transducer. Probe light is incident at an angle θ on its curved surface, and focused onto the opaque film. The tomographic picosecond strain-pulse profiling technique is based on Brillouin scattering of the probe light by the acoustic waves transmitted to the transparent medium [23–30]. When quasi-monochromatic plane-wave probe light is reflected from a plane-wave longitudinal ultrasonic pulse in a photoelastic medium, the amplitude of the reflected light is proportional to the amplitude of the acoustic strain component at the Bragg scattering condition for the acoustic wavelength in question:

$$\Lambda = \lambda/(2n\cos\theta), \tag{1}$$

* Corresponding author.
E-mail address: mtomoda@eng.hokudai.ac.jp (M. Tomoda).

https://doi.org/10.1016/j.pacs.2023.100567
Received 15 July 2023; Received in revised form 10 October 2023; Accepted 25 October 2023
Available online 29 October 2023

where Λ is the wavelength of the acoustic wave, λ is the wavelength of the probe light in air (or, strictly speaking, in vacuum), θ is the angle between the wave vector of the probe light in the medium and that of the acoustic wave, and n is the refractive index of the medium at the probe optical wavelength [31]. The reflected probe light scattered from the strain pulse interferes with reflected light components from surfaces and interfaces in the sample. The detected light includes information on the amplitude and phase of the acoustic wave component at wavelength Λ appropriate to angle θ. At this acoustic wavelength, time-domain Brillouin oscillations in optical reflectivity occur at the Brillouin oscillation frequency f_B:

$$f_B = \frac{2nv\cos\theta}{\lambda}, \tag{2}$$

where v is the longitudinal sound velocity. We measure the optical reflectivity changes containing these oscillations as a function of θ, and thereby reconstruct the strain pulse shape as a function of the depth z by use of an inverse method known as singular value decomposition [32–37]. By repeating the inversion process for a sequence of delay times between the pump and the probe optical pulses, a strain propagation movie can be built up.

2.2. Forward problem

When strain $\eta_{33}(z)$ is distributed in the depth (z) direction in a transparent material, the relative reflectivity change of s-polarized probe light pulse incident at angle θ inside the transparent medium on the opaque film is given by

$$\begin{aligned}\frac{\delta R}{R} &= 2\mathrm{Re}\left(\frac{\delta r}{r}\right)\\ &= \mathrm{Im}\left\{\frac{2\pi P_{12}}{\sqrt{\varepsilon_1}\lambda\cos\theta}\int_0^\infty \eta_{33}(z)\right.\\ &\quad\left.\times\left[\exp\left(-i\frac{2\pi\sqrt{\varepsilon_1}z\cos\theta}{\lambda}\right)+r\exp\left(i\frac{2\pi\sqrt{\varepsilon_1}z\cos\theta}{\lambda}\right)\right]^2 dz\right\},\end{aligned} \tag{3}$$

where

$$r = \frac{\cos\theta-\sqrt{\varepsilon_2/\varepsilon_1-\sin^2\theta}}{\cos\theta+\sqrt{\varepsilon_2/\varepsilon_1-\sin^2\theta}} \tag{4}$$

is the reflection coefficient of s-polarized light at the interface, ε_1 and ε_2 are the complex dielectric constants of the transparent medium and the opaque film, respectively, λ is the central wavelength of the probe light in air, $P_{12} = \partial\varepsilon_1/\partial\eta_{33}$ is the photoelastic constant of the transparent medium, and $z = 0$ is set at the interface [21,38,39]. Changes in ε_2 and any effects of finite substrate thickness are ignored. The reflectivity R and the amplitude reflection coefficient r are related by $R = |r|^2$. Similar equations for p-polarized light exist, but lead to more complex analysis owing to their dependence on two photoelastic constants [21].

2.3. Inverse problem

Equation (3) represents an integral transformation from the strain depth profile $\eta_{33}(z)$ to the relative reflectivity change $\delta R/R$ at probe incident angle θ; this transformation can be categorized as a 1st-kind Fredholm integral equation. We regard this integral as the forward problem and solve the inverse problem that outputs the strain distribution $\eta_{33}(z)$ from the input relative reflectivity change $\delta R(\theta)/R(\theta)$ by use of singular value decomposition, which is widely used to solve inverse problems.

We rewrite the forward problem integration of Eq. (3) as

$$p(\theta) = \int_0^L G(z,\,\theta)\,\eta(z)\,dz, \tag{5}$$

where the data vector $p(\theta)$ corresponds to the relative reflectivity change $\delta R(\theta)/R(\theta)$, $G(z,\,\theta)$ is the detection kernel of this transformation, $\eta(z)$ is the object vector corresponding to the strain distribution $\eta_{33}(z)$, and L is set to a finite length for $\eta(z > L) = 0$. This type of integral transformation does not have an inverse transformation in general. A discrete approximation can be implemented in Eq. (5):

$$p(\theta_j) = \sum_{i=1}^{N} G(z_i,\,\theta_j)\,\eta(z_i)\,\Delta z_i, \tag{6}$$

where $p(\theta_j)$ is a vector of order M, $\eta(z_i)$ is a vector of order N, and $G(z_i,\theta_j)$ is a matrix of order $M\times N$.

The Kernel is decomposed to the unique form

$$G(z,\,\theta) = \sum_i U_i(\theta)\mu_i V_i(z), \tag{7}$$

where $U_i(\theta)$ and $V_i(z)$ represent orthonormal bases in the θ and z domains, respectively, and μ_i are singular values ($\mu_i \geq 0$). The singular functions are chosen so that

$$\int_\theta U_k(\theta)U_i(\theta)\,d\theta = (U_k,U_i)_\theta = \delta_{i,k}, \tag{8}$$

$$\int_0^L V_k(z)V_i(z)\,dz = (V_k,V_i)_z = \delta_{i,k}, \tag{9}$$

where the form (φ,ϑ) represents an inner product $(\varphi,\vartheta)_\xi \equiv \int\varphi(\xi)\vartheta(\xi)d\xi$, and $\delta_{i,j}$ is Kronecker delta. If the set of functions $V_k(z)$ is complete, then

$$\eta(z) = \sum_k A_k V_k(z), \tag{10}$$

where the weighting coefficients A_k have to be found. By combining Eqs. (5)–(10), one obtains

$$\begin{aligned}p(\theta) &= \int_0^L G(z,\theta)\eta(z)\,dz = \sum_i U_i(\theta)\mu_i\sum_k A_k\int_0^L V_i(z)V_k(z)dz\\ &= \sum_i A_i\mu_i U_i(\theta).\end{aligned} \tag{11}$$

Multiplying by $U_k(\theta)$ and integrating the result with respect to θ, one obtains

$$\int_\theta p(\theta)U_k(\theta)d\theta = \sum_i A_i\mu_i\delta_{i,k} = A_k\mu_k. \tag{12}$$

The weighting coefficients become

$$A_k = \frac{1}{\mu_k}\int_\theta p(\theta)U_k(\theta)d\theta = \frac{(p,U_k)_\theta}{\mu_k}. \tag{13}$$

Finally, the depth profile can be found as follows:

$$\eta(z) = \sum_k A_k V_k(z) = \sum_k\frac{1}{\mu_k}\int_\theta p(\theta)U_k(\theta)d\theta\cdot V_k(z) = \sum_k\frac{(p,U_k)_\theta}{\mu_k}V_k(z). \tag{14}$$

This equation shows that the strain profile $\eta(z)$ can be expressed as a linear superposition of orthonormal functions $V_k(z)$ weighted by the coefficients A_k.

The above equations can be rewritten in matrix form: Eq. (6) becomes

$$\boldsymbol{p} = \mathbf{G}\cdot\boldsymbol{q}, \tag{15}$$

where $\boldsymbol{p}$ is a column vector containing the discrete values of the input data, $\boldsymbol{p} = [p(\theta_1), p(\theta_2), \ldots, p(\theta_M)]^T$, $\boldsymbol{q}$ is a column vector containing the discrete values of the object data, $\boldsymbol{q} = [\eta(z_1), \eta(z_2), \ldots, \eta(z_N)]^T$, and $\mathbf{G}$ is an $M\times N$ matrix approximating $G(z,\theta)$. By singular decomposition (Eq. (7)), $\mathbf{G}$ may be expressed as

$$\mathbf{G} = \mathbf{U}\cdot\mathbf{W}\cdot\mathbf{V}^T, \tag{16}$$

where $\mathbf{V}$ and $\mathbf{U}$ are symmetric orthogonal matrices of order $N\times N$ and $M\times M$, respectively, and $\mathbf{W}$ is an $M\times N$ matrix whose diagonal

elements are singular values $\mu_1 \geq \mu_2 \geq \cdots \geq \mu_N \geq 0$, under the condition $N \leq M$:

$$\mathbf{W} = \begin{pmatrix} \mu_1 & & & \\ & \mu_2 & & 0 \\ & & \ddots & \\ & & & \mu_N \end{pmatrix}. \tag{17}$$

Here, the object vector $\boldsymbol{q}$ is expressed in the form

$$\boldsymbol{q} = \left(\mathbf{V} \cdot \mathbf{W}^{-1} \cdot \mathbf{U}^T\right) \cdot \boldsymbol{p}, \tag{18}$$

which corresponds to Eq. (14).

The weighting coefficients A_k in Eq. (13) are strongly dependent on μ_k^{-1}. If μ_k takes an extremely small value, the k-th term contributes as a reciprocal to large amplification factors in the solution profile $\eta(z)$. Noise, experimental errors, and systematic errors including discretization and rounding cause fluctuations in the internal product $(p, U_k)_\theta$, which can catastrophically change the solution profile $\eta(z)$ in the case of extremely small μ_i. To avoid these ill-conditioned terms, we simply use a suitable number K of 'good' singular functions. We arrange all N singular values in order from the top to the bottom values, $\mu_1 \geq \mu_2 \geq \cdots \geq \mu_K \geq \mu_{K+1} \geq \cdots \geq \mu_N \geq 0$, and set $\mu_{K+1} = 0$, ..., $\mu_N = 0$ (rank truncation). The rank truncation reduces errors, but imposes a limit on spatial resolution. There are several criteria used to select a suitable number of singular functions V_K [33]. To do this we plot the residual

$$\begin{aligned} y &= \left\{ \int_\theta \left[p_K(\theta) - p(\theta)\right]^2 d\theta \right\}^{1/2} \\ &= \left\{ \int_\theta \left[\int_0^L G(z,\theta) \eta_K^{\text{trunc}}(z) dz - p(\theta) \right]^2 d\theta \right\}^{1/2} \end{aligned} \tag{19}$$

as a function of the modulus of the reconstructed strain

$$x = |\eta_K^{\text{trunc}}(z)| = \left\{ \int_0^L [\eta_K^{\text{trunc}}(z)]^2 dz \right\}^{1/2} \tag{20}$$

for all K. Here, $p_K(\theta)$ is the solution of the forward problem of Eq. (3) using $\eta_K^{\text{trunc}}(z)$, which is the reconstructed solution up to the truncated Kth term. A typical "L" shape arises (see Appendix). The optimum K can be found at the edge of the "L", which corresponds to the maximum of d^2y/dx^2.

We execute the inverse-problem process for each delay time independently, and then adopt the most commonly attained maximum K value for the full set of angle-time scan data $p(\theta, t) = \delta R(\theta, t)/R(\theta)$.

3. Experimental setup

We have implemented three major changes compared to the previous investigation using this tomographic approach in order to enhance both the spatial resolution and the ease of measurement [22]:

- We use automated angle scanning. Previously it was necessary to realign the optics after every incidence-angle change. This allows us to increase the number of probed angles, reduce the measurement time and keep the optical beams focused at a single unique point on the sample. Subtraction of a constant background before the inverse calculation is unnecessary. (In our previous work, variation in this background with angle required such subtraction.)
- We use visible light at wavelength 415 nm for the probe, whereas previously we used infrared light at 830 nm. This improves the spatial resolution.
- We make use of coaxial pump and probe beams focused at the centre of the sample from the same side. Previously the pump beam was focused from the transducer film side. This facilitates the alignment.

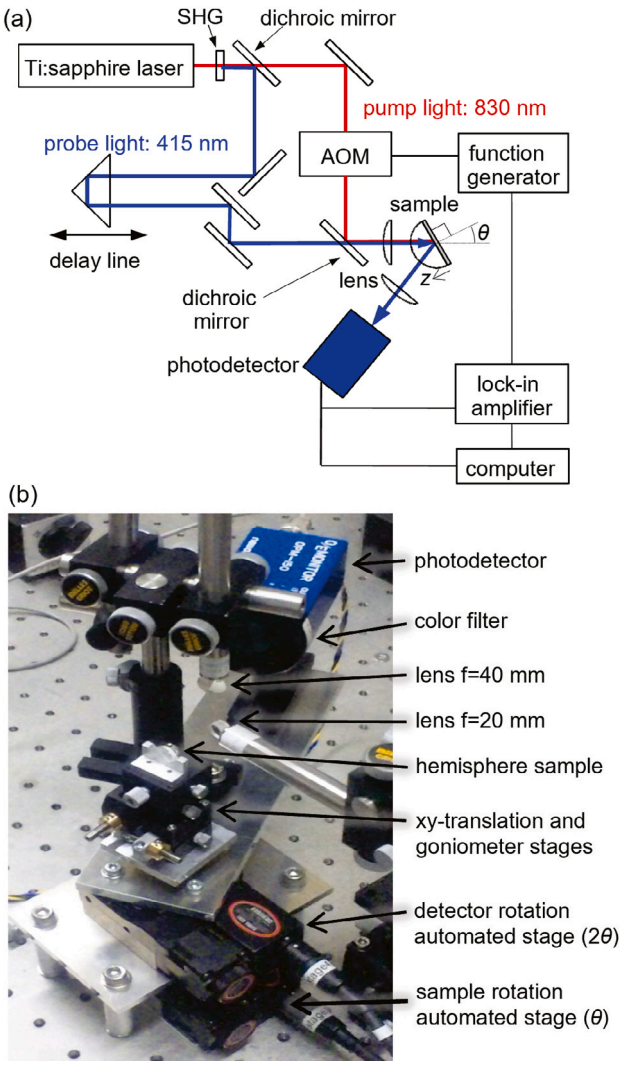

Fig. 1. (a) Optical setup. The sample is an Al-coated BK7-glass hemisphere. The sample and photodetector are set on automated θ-2θ rotation stages. SHG: second harmonic generation crystal, AOM: acousto-optic modulator. (b) Photo of the samples and stages.

3.1. Sample

The sample is an isotropic BK7 glass hemisphere of radius 5 mm coated on its flat face with a polycrystalline Al film of thickness $d_2 = 400$ nm. Aluminum is a widely used transducer film in picosecond ultrasonics, with an acoustic impedance close to that of BK7 glass. A broad spectrum of acoustic frequencies up to and above ~100 GHz is generated [40]. The 5-mm radius of the glass hemisphere is chosen to be smaller than the focal length of the focusing lens ($f = 20$ mm).

3.2. Measurement

We use a conventional picosecond ultrasonics technique involving a femtosecond pulsed laser and a mechanical delay stage, as shown schematically in Fig. 1(a). The pump and probe pulses originate from a Ti:sapphire mode-locked laser, whose centre wavelength is 830 nm, pulse duration (full width at half maximum; FWHM) ~100 fs and repetition rate 76 MHz. The pump pulses at wavelength 830 nm are modulated at 1 MHz with an acousto-optic modulator for lock-in detection. The probe beam, frequency-doubled by a second harmonic generation crystal (β-BaB_2O_4), is reflected by a corner-cube set on a linear, automated mechanical stage to provide a variable delay.

The pump and probe beams are overlapped at a dichroic mirror and focused by the same lens (f = 20 mm) onto the Al-glass interface from the hemisphere-glass side with s-polarized optical incidence. The pump beam incident pulse energy is Q = 1.0 nJ, and the FWHM spot size is ~20 μm for the case of normal incidence. This produces an instantaneous maximum temperature rise of ~10 K and a maximum steady state rise of ~50 K in the sample [20,21,41]. The probe beam pulse energy is 0.01 nJ, and the FWHM spot size is ~10 μm at normal incidence. The hemisphere sample is set on automated coaxial θ-2θ rotation stages: when angle scanning, the sample rotates by θ and the detector by 2θ, as shown in Fig. 1(b). The pump and probe beam spots are carefully aligned to focus on the centre of the hemisphere sample, which is also aligned to lie on the rotational axes of the θ-2θ stages. After reflection from the sample, the probe light passes through a lens (f = 40 mm) and a blue color filter that blocks the reflected pump beam. It is then detected at a photodetector (a Si PIN photodiode). The output of the photodetector is connected to a lock-in amplifier synchronized to the chopping frequency, and its output is monitored. Relative reflectivity changes $\delta R(\theta,t)/R(\theta)$ are recorded as a function of θ and t. For a fixed t, the rotational stage is scanned in the range θ = 10° to 75° at 2°/s with a step of 0.2°. The lower angle of 10° is chosen to avoid blocking the reflected probe beam with the focusing lens. The upper angle of 75° is determined by the low reflectivity change above this value and by alignment considerations. The delay time increment is chosen to be 5 ps. One complete measurement over all delay times takes 8.5 h.

The pump and probe laser intensities on the sample vary with the angle of incidence: for larger angles the reflectivity increases, and the major axis of the elliptical spot becomes longer. Before the inversion process to calculate the strain distribution, we normalize the reflectivity change as follows: the absorbed intensity at the sample is given by $P_{\mathrm{pump}} \propto (1 - R_{\mathrm{pump}})$ where $R_{\mathrm{pump}}(\theta)$ is the reflectivity of the sample calculated from the Fresnel equations (making use of refractive indices of BK7 glass, $n_{1,\mathrm{pump}}$ = 1.51, and of the Al film, $n_{2,\mathrm{pump}}$ = 2.75+8.31i, for the pump beam at λ_{pump} = 830 nm [42,43]), so we divide the measured $\delta R/R$ by $(1 - R_{\mathrm{pump}})\cos\theta$, which in addition accounts for the angle-dependent elliptical pump spot shape. The relative reflectivity change $\delta R/R$ of the probe beam is obtained in experiment by making use of the DC signal from the photodetector as well as by monitoring the lock-in output. Before presenting the experimental results we will first give the results of simulations for the same sample and conditions as in the experiment in order to illustrate the analysis technique.

4. Simulations and tomographic strain-pulse reconstruction

4.1. Strain generation and propagation

We conducted a time-domain simulation of the strain pulse generation and its one-dimensional (1D) propagation to check the reconstruction process in the absence of experimental errors. For the simulation we chose the pump beam spot size to be 20 μm (FWHM), with propagation depths up to 4 μm. We solved the acoustic wave equations with appropriate initial conditions by use of a finite-difference method [41].

Strain pulse generation is governed by a linear thermoelastic process, given that the optical pulse energy is much lower than the sample damage threshold. When the pump light, incident from the glass side, is focused onto the Al-glass interface, optical energy is initially absorbed in Al approximately within the optical penetration depth ~8 nm (obtained from the refractive index n_2). Diffusing excited electrons then transport this energy to a depth $\zeta_e \approx (\kappa/g)^{1/2} \approx$ 22 nm [44], before the lattice is heated through electron–phonon coupling (described by constant $g = 4.9 \times 10^{17}$ W m^{-3} K^{-1} [40] for Al with thermal conductivity κ = 237 W m^{-1} K^{-1} [45]) over a timescale ~1 ps, producing an approximately exponential heating profile in the depth direction. All the physical parameters used in this section are listed in Table 1.

Thermal stress then produces two strain pulses, one propagating towards the Al-glass interface and the other propagating towards the opposite Al-film free surface. The first pulse is partly transmitted to the glass as a unipolar strain pulse, and the second, also unipolar, strain pulse propagates towards and is reflected at the free Al surface. It is then in turn partially transmitted to the glass, and is again partially reflected. The strain pulse reflectance and transmittance follow the acoustic Fresnel equations $r_{ac} = (Z_2 - Z_1)/(Z_2 + Z_1) \approx 0.055$ and $t_{ac} = 2Z_1/(Z_2 + Z_1) \approx 0.945$, where $Z_2 = \rho_2 v_2 = 17.3 \times 10^6$ Pa s m^{-3} [45] and $Z_1 = \rho_1 v_1 = 15.5 \times 10^6$ Pa s m^{-3} [42] are the acoustic impedances of Al and BK7 glass, respectively.

The strain pulse propagating towards the Al-film free surface is inverted on reflection because $Z_{\mathrm{air}} \ll Z_2$, and subsequently enters the glass with a delay with respect to the first strain pulse equal to the round-trip time $\Delta t = 2d_2/v_2 \simeq$ 125 ps. The first and the second strain pulses of respective amplitudes A_1 and A_2 have opposite signs, and the ratio of their amplitudes is $A_1/A_2 = -1/(1 + r_{ac}) \approx -0.95$, ignoring ultrasonic attenuation in the Al film. The shape of the first two strain pulses in the absence of ultrasonic attenuation is shown in Fig. 2(a) and in the inset of Fig. 2(d), assuming an exponential heat deposition profile immediately following electron diffusion, as outlined above. The right-hand, negative pulse produces the first echo and the left-hand, positive pulse produces the second echo. The third pulse, which makes two round trips inside the Al film, is in contrast weaker by a factor $A_3/A_2 = -r_{ac} \approx -0.055$. Likewise for subsequent pulses.

With the above electron diffusion depth ζ_e, one can estimate the maximum amplitude of the generated strain pulse in the Al film [21],

$$\eta_0 = \frac{3B_2\beta_2(1 - R_1)(1 - R_2)Q}{A\zeta_e c_2 \rho_2^2 v_2^2} \sim 4 \times 10^{-4}, \tag{21}$$

where R_1 = 0.04 and R_2 = 0.81 are optical pump beam reflectivities at the air-glass and Al-glass interfaces, respectively, A is the effective pump spot area (see below) and Q = 1 nJ is the pump pulse energy. The physical properties of Al are taken as follows: c_2 = 931 J kg^{-1} K^{-1} is the specific heat capacity, ρ_2 = 2690 kg m^{-3} is the density, $\beta_2 = 23.0 \times 10^{-6}$ K^{-1} is the linear thermal expansion coefficient, B_2 = 77.7 GPa is the bulk modulus, v_2 = 6420 m s^{-1} is the longitudinal sound velocity [45]. The pump spot area is calculated as $A = \pi w_{\mathrm{pump}}^2/2$ using a Gaussian pump beam ($1/e^2$ intensity) half-width w_{pump}=(20 μm)/$\sqrt{2\ln 2}$ = 17 μm from the FWHM pump beam spot size of 20 μm. At these levels of strain, the propagation of the strain pulses is expected to be linear.

For the propagation in the hemisphere, the longitudinal sound velocity for BK7 glass v_1 = 6048 m s^{-1} is calculated from the Young's modulus 82 GPa, Poisson's ratio 0.206, and density ρ_1 = 2510 kg m^{-3} [42]. Frequency-dependent ultrasonic attenuation distorts this strain pulse as it propagates, so we take this into account by use of the following literature f-dependent attenuation constants: $\alpha_1 = 140 \cdot f^2$ m^{-1} and $\alpha_2 = 860 \cdot f^2$ m^{-1}, where f is the frequency in GHz [46]. Since the ultrasonic attenuation of Al is not negligible at the frequencies in question, the amplitude of the first pulse becomes significantly higher than that of the second, as shown by the image plot of Fig. 2(a) as well as by the example of the green solid line in Fig. 2(d) for a delay time of t = 300 ps. As the pulses propagate they become broadened by the frequency-dependent ultrasonic attenuation (see the Supplementary Movie).

4.2. Reflectivity changes

The predicted normalized reflectivity variation is shown by the image plot in Fig. 2(b) as a function of delay time and angle, exhibiting characteristic Brillouin oscillations at frequencies f_B in the range 11.5–43.9 GHz. This variation is calculated using the refractive indices $n_1 = \sqrt{\varepsilon_1}$ = 1.529 and $n_2 = \sqrt{\varepsilon_2}$ = 0.523+5.024i for the probe beam at λ = 415 nm by use of Eqs. (3) and (4) [42,43]. The photoelastic constant of BK7 glass is assumed to be positive [47].

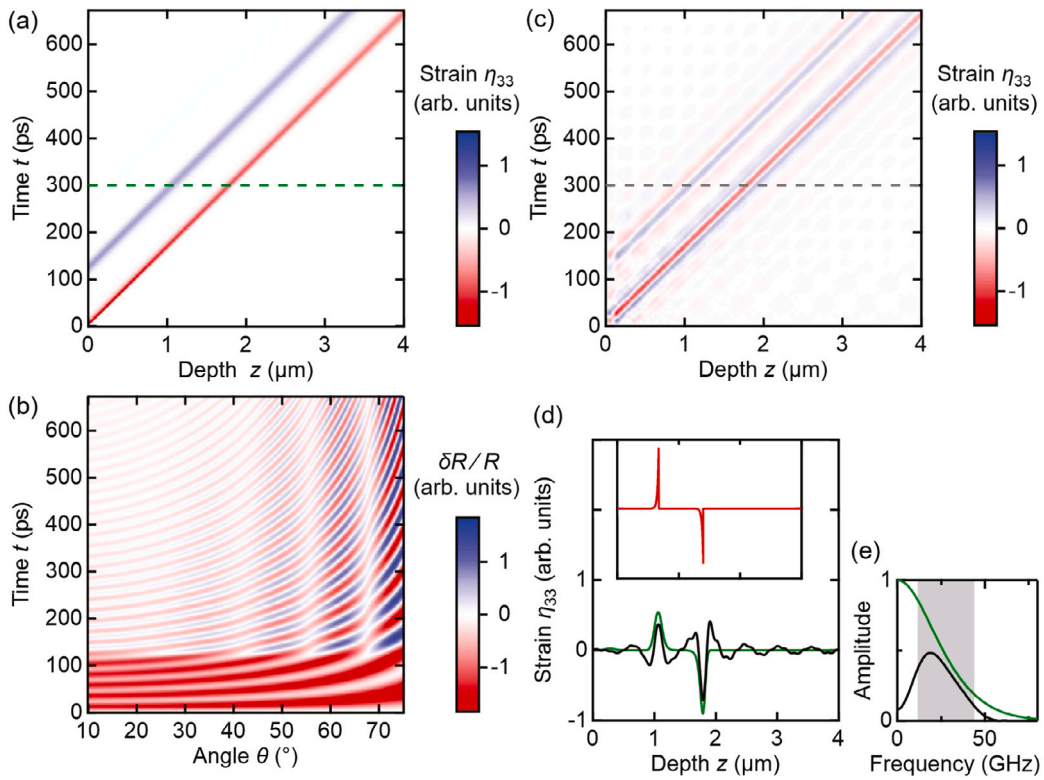

Fig. 2. (a) Simulated strain $\eta_{33}(z,t)$. (b) Image plot of the simulated relative reflectivity change $\delta R(\theta,t)/R(\theta)$. (c) Reconstructed normalized strain $\eta_{33}(z,t)$. (d) Normalized simulated (green solid line) and reconstructed (black solid line) strain distributions at t = 300 ps. Inset: the red curve shows the analytically calculated normalized strain pulse shape in the absence of ultrasonic attenuation, plotted with the same scale in the depth direction. (e) Frequency spectrum of the simulated (green solid line) and reconstructed (black solid line) first strain pulse when it reaches a depth of 1.8 μm, corresponding to $t \sim$ 300 ps, plotted on the same scale. The shaded region corresponds to the tomographically probed frequency range 11.5–43.9 GHz. The scales for strain in (a), (c) and (d) are identical.

Table 1
List of physical parameters used in the strain propagation and reflectance change simulations and strain-pulse reconstructions.

λ_{pump}	830 nm	wavelength of pump light
λ	415 nm	wavelength of probe light
d_2	400 nm	thickness of Al film
v_2	6420 m s^{-1}	longitudinal sound velocity of Al [45]
ρ_2	2690 kg m^{-3}	mass density of Al [45]
c_2	931 J kg^{-1} K^{-1}	specific heat capacity of Al [45]
β_2	23.0 × 10^{-6} K^{-1}	linear thermal expansion coefficient of Al [45]
B_2	77.7 GPa	bulk modulus of Al [45]
g	4.9 × 10^{17} W m^{-3} K^{-1}	electron–phonon coupling constant of Al [40]
κ	237 W m^{-1} K^{-1}	thermal conductivity at 300 K [45]
α_2	860 · f^2 m^{-1}	ultrasonic attenuation coefficient of Al, where f is frequency in GHz [46]
n_2	0.523 + 5.024i	complex refractive index of Al at 415 nm [43]
$n_{2,pump}$	2.75 + 8.31i	complex refractive index of Al at 830 nm [43]
v_1	6048 m s^{-1}	longitudinal sound velocity of BK7 [42]
ρ_1	2510 kg m^{-3}	mass density of BK7 [42]
α_1	140 · f^2 m^{-1}	ultrasonic attenuation coefficient of BK7, where f is frequency in GHz [46]
n_1	1.529	refractive index of BK7 at 415 nm [42]
$n_{1,pump}$	1.510	refractive index of BK7 at 830 nm [42]

The reflectivity change shows an abrupt transformation at delay time t = 125 ps when the second strain pulse enters the glass. After this time the amplitude of the reflectivity changes depend on incident angle because of the optical interference between the probe light reflected from the first and second strain pulses. The effect of the much smaller third and higher-order strain pulses is negligible on the reflectivity.

4.3. Tomographic strain-pulse reconstruction

The reconstruction method is based on Eqs. (14) and (18). We used 326 angles (10°-75° with a step of 0.2°) to calculate 326 points in space over 5 μm with a step of 15.385 nm, taking the required physical parameters as in the simulation described above. The number of singular values μ_i used in the calculation is K = 55. This value was chosen by inspecting the value of d^2y/dx^2 in Eq. (19).

The spatiotemporally reconstructed strain distribution, shown on the normalized plot of Fig. 2(c), shows the expected propagation at the constant velocity v_1, similar to the predicted behavior in Fig. 2(a) (see also the Supplementary Movie). The amplitude of the first two reconstructed strain pulses are opposite to one another, as expected, as shown by the black curve in Fig. 2(d). Although the predicted pulse shapes are unipolar, the reconstructed shapes show some spatial oscillations because of the restricted range of optical incidence angles: the acoustic wavelength measured by the probe beam at an incident angle θ is $\Lambda = \lambda/(2n\cos\theta)$ (see Eq. (1)), and the implemented angle range θ = 10°-75° corresponds to Λ = 138–524 nm or f_B = 11.5–43.9 GHz. The lack of higher-angle components degrades the spatial resolution, and the lack of lower-angle components leads to the spatial oscillations [22]. The spectrum of the first reconstructed strain pulse when it reaches a depth of 1.8 μm, corresponding to $t \sim$ 300 ps, is shown in Fig. 2(e) by the black curve, exhibiting a broad frequency distribution centred around 10–40 GHz. In comparison with the equivalent spectrum of the calculated first strain pulse, shown by the green curve, there is significant amplitude reduction and spectral narrowing owing to the limited range of tomographically probed frequencies (shaded area).

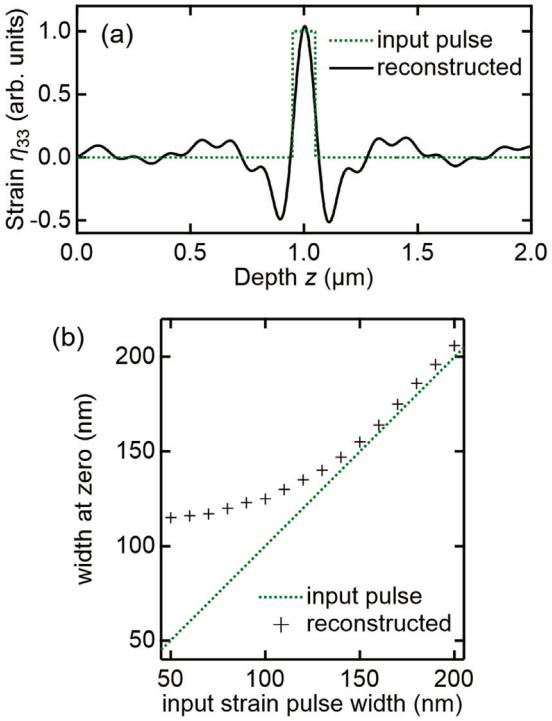

Fig. 3. (a) Input top-hat strain pulse (dotted green line) with a width of 100 nm, centred at a position of 1.0 μm, plotted together with its reconstructed pulse (black solid line) as a function of depth in BK7 glass. (b) Reconstructed strain pulse width (shown by crosses), sampled at the zero-strain level, plotted as a function of the input top-hat strain pulse width. The dotted green line shows the case of an ideal reconstruction.

4.4. Strain resolution

To check the spatial resolution of the method, the width of the reconstructed strain pulses is calculated for a series of top-hat shaped strain pulses of different spatial widths, and the reconstructed pulses are calculated using the same forward and inverse problem parameters as in the simulations of Section 4. Single top-hat strain pulses centred at 1.0 μm are set in the BK7 glass, as shown by the example of a 100 nm width in Fig. 3(a). We record the width of each reconstructed pulse at the zero-strain level. When the top-hat pulse width is wider than ~150 nm, the reconstructed pulse width takes on a similar value. But when the top-hat pulse width becomes progressively less than 150 nm, the reconstructed pulse width tends to ~120 nm. This 120-nm value therefore represents a reasonable measure of the limiting spatial resolution for strain, which is slightly less than the minimum acoustic wavelength, ~138 nm, probed, and equal to ~30% of the optical probe wavelength λ in air (or ~45% of the probe wavelength λ/n in BK7 glass).[1] The corresponding resolution in Ref. [22] is 250 nm.

5. Experimental results and discussion

5.1. Experimental results

The measured normalized reflectivity change as a function of the incident angle θ and delay time t is shown in Fig. 4(a), which is very similar to that calculated in Fig. 2(b). Background signals caused by temperature changes are subtracted before analysis. The spatiotemporally reconstructed strain as a function of delay time is shown by the image plot of Fig. 4(b) (see also the Supplementary Movie). The number of singular values $K = 55$ is chosen by the same protocol as for the simulation, and gave the same result for K. This reconstructed strain distribution at $t = 300$ ps is shown in Fig. 4(c). The general agreement with the simulation in Fig. 2(d) is reasonable considering the presence of experimental noise. The experimental amplitude spectrum of the first reconstructed strain pulse when it reaches a depth of 1.8 μm, corresponding to $t \sim 300$ ps, is shown in Fig. 4(d) by the black curve, exhibiting a broad frequency distribution centred around 10–40 GHz similar to that previously reconstructed by simulation in Fig. 2(e). The sound velocity of the substrate glass measured from the reconstructed images, 6080 ± 30 m s^{-1}, is similar to the literature value of 6048 m s^{-1} used in the simulation. The sound velocity v_1 is not used in the reconstruction process, although the refractive index is necessary. The derived value of v_1 is different from that, 5860 ± 30 m s^{-1}, reported

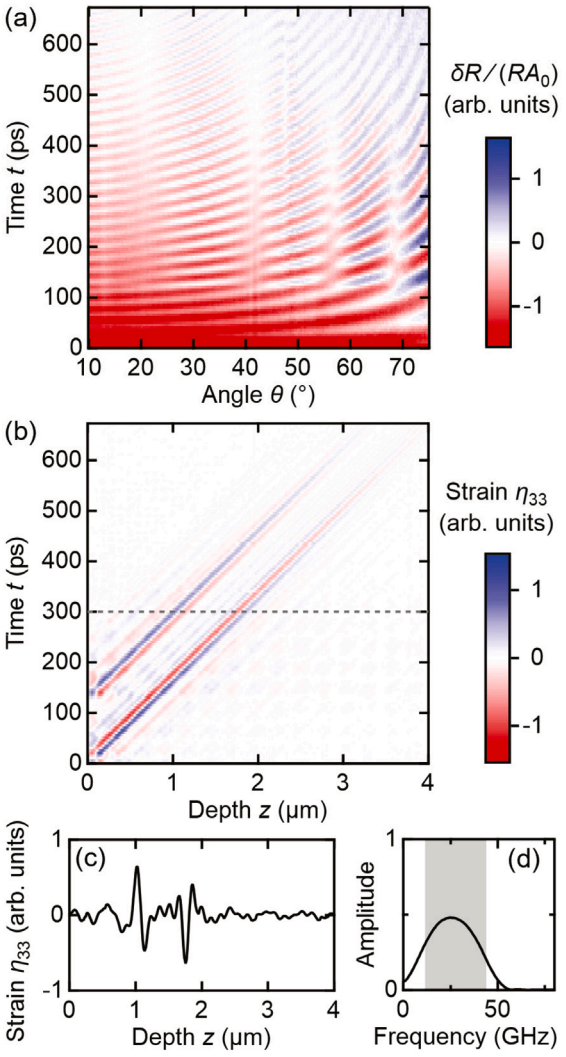

Fig. 4. (a) Image plot of the measured relative reflectivity change $\delta R(\theta,t)/R(\theta)$, normalized by $A_0 \propto (1 - R_{\text{pump}})\cos\theta$, where R_{pump} is a reflectivity of pump light and the term $\cos\theta$ is included to compensate for the elliptical shape of the pump spot. (b) Reconstructed normalized strain $\eta_{33}(z,t)$. (c) Reconstructed normalized strain distribution at $t = 300$ ps. (d) Frequency spectrum of the reconstructed strain when it reaches a depth of 1.8 μm, corresponding to t~300 ps. The shaded area corresponds to the tomographically probed frequency range $f = 11.5$–43.9 GHz. The scales for strain in (b) and (c) are identical.

[1] Since strain is an amplitude and not an intensity, it can take positive or negative values, so the discussion of spatial resolution is distinct from that of the more common case of intensity resolution.

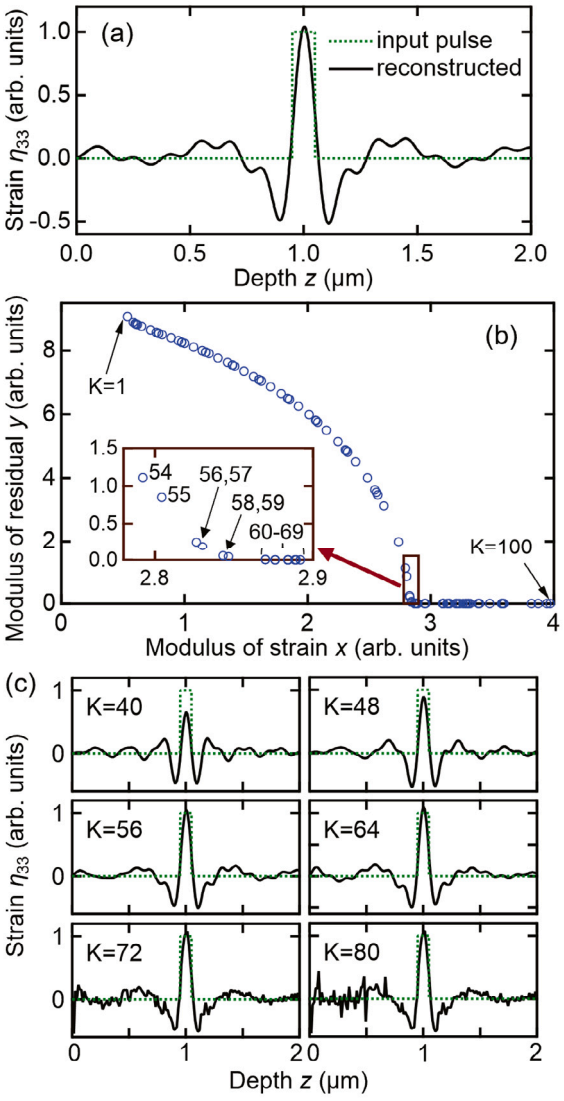

Fig. 5. (a) An example of the inverse calculation when the number of singular functions is $K = 56$ (optimum value). The input top-hat strain pulse (dotted green line) of width 100 nm and centred at a depth of 1.0 μm is plotted together with its reconstructed pulse (black solid line) as a function of depth. (b) Plot of the modulus of the residual y vs the modulus of the strain x. The edge of the "L" shape corresponds to the point with optimum K. Inset: zoomed-in view around the edge of the "L" shape. (c) Some examples of reconstructed pulse shapes when changing the number of singular functions K.

in our previous publication [22], presumably because of the different substrate glass used.

5.2. Discussion

Although we have included ultrasonic attenuation in our simulation, there are other forms of possible attenuation. Acoustic diffraction is not included in the 1D simulation shown in Fig. 2(a). In the present geometry, the acoustic wavelength, $\Lambda \sim 100$ nm, on the order of the spatial extent of the acoustic pulse in the depth direction, is small compared to its lateral extent $\sim 2w_{\mathrm{pump}} = 34$ μm. The corresponding acoustic diffraction angle is $\phi = \Lambda/(\pi w_{\mathrm{pump}}) \sim 2 \times 10^{-3}$ rad $\sim 0.1°$, which has a negligible influence over the range of delay times used in our experiment. Another attenuation effect not included in the 1D simulation is the limited spatial overlap between the reflected and scattered probe light. This effect, arising from the finite spot-size, becomes larger at higher angles of incidence and as the strain pulse becomes further away from the Al-glass interface. A final attenuation effect not included in the 1D simulation is the effect of the finite optical coherence length of the probe pulse [23,29,48]. Simple estimates of these latter two effects suggest that they should not have a particularly large influence ($\lesssim$15%) in the present experimental geometry at the maximum depth, ~4 μm, probed. A more detailed analysis of these effects is beyond the scope of this work. The ultrasonic attenuation observed in experiment is significantly larger than that predicted in the simulation, as can be understood by comparing Figs. 2(c) and 4(b). Differences in the detailed composition of the glass may be responsible for this, since the attenuating effects of acoustic diffraction, beam overlap and optical coherence are all expected to be relatively small.

6. Conclusions

In conclusion, we have described an automated tomographic measurement technique for visualizing GHz longitudinal ultrasonic strain pulse propagation with improved spatial resolution and measurement speed. Simulations were used to check the quality of the reconstruction, and gave fair agreement with experiment.

At present the technique is restricted to 1D probing of longitudinal strain in homogeneous, isotropic and transparent solids, making use of a hemispherical substrate. This need could be circumvented by means of an automated angle-scan technique based on a lateral beam scan over a high numerical-aperture objective lens [30]. This would open up the possibility of extending the technique to 3D strain-pulse imaging in plate-shaped samples by combination with probe-beam 2D lateral scanning. It may also be possible to apply the method to imaging picosecond shear strains in solids by use of similar angle scanning and suitable optical polarization [21]. If the spatial distribution of the sound velocity is known it may also be possible to probe 3D distributions of optical refractive index. Finally, this tomographic technique extended to sub-picosecond temporal resolution could be used to reconstruct other ultrafast transient fields that couple to the dielectric constant, such as carrier or temperature distributions, or to image nonlinear optical pulse propagation.

Declaration of competing interest

The authors declare the following financial interests/personal relationships which may be considered as potential competing interests: Motonobu Tomoda reports financial support was provided by the Japan Society for the Promotion of Science. Osamu Matsuda reports financial support was provided by the Japan Society for the Promotion of Science. Roberto Li Voti reports financial support was provided by the Japan Society for the Promotion of Science. Oliver B. Wright reports financial support was provided by the Japan Society for the Promotion of Science.

Data availability

Data will be made available on request.

Acknowledgment

We acknowledge Grants-in-Aid for Scientific Research from the Japan Society for the Promotion of Science.

Appendix A. Number of singular functions

This Appendix shows how the singular function number K affects the reconstructed strain shape, providing supplementary information to that in Section 2.3. Figure 5 shows the results of calculations when choosing a top-hat strain pulse of width 100 nm and centred at a depth 1.0 μm as a test input function (the green dotted line in Fig. 5(a)). The parameters used in the calculations of the forward problem (Eq. (3)) and the inverse problem (Eqs. (14) or (18)) are listed together with other parameters used in this paper in Table 1. The reconstructed strains are expressed as a superposition of singular functions. Figure 5(b) shows a plot of the modulus of the residual y vs the modulus of the strain x for different K, where y and x are defined in Eqs. (19) and (20), respectively. The form the reconstructed strain for optimum K = 56, corresponding to the maximum of d^2y/dx^2, is shown in Fig. 5(a). If K is less than the optimal value, the reconstructed strain does not reproduce the input function as well. If K is greater than the optimal value, the reconstructed strain includes components with higher spatial frequencies, and the amplitude of the reconstructed strain increases, although the reconstruction does exhibit smaller residuals. Examples of the reconstructed strain at representative values of K are shown in Fig. 5(c).

Appendix B. Supplementary data

Supplementary material related to this article can be found online at https://doi.org/10.1016/j.pacs.2023.100567.

References

[1] G. Gunarathne, J. Szilard, A new stroboscope for schlieren and photoelastic visualization of ultrasound, Ultrasonics 21 (4) (1983) 188–190, http://dx.doi.org/10.1016/0041-624X(83)90076-8.

[2] C. Ying, S. Zhang, J. Shen, Scattering of ultrasound in solids as visualized by the photoelastic technique, J. Nondestruct. Eval. 4 (1984) 65–73, http://dx.doi.org/10.1007/BF00566398.

[3] S. Washimori, T. Mihara, H. Tashiro, Investigation of the sound field of phased array using the photoelastic visualization technique and the accurate fem, Mater. Trans. 53 (4) (2012) 631–635, http://dx.doi.org/10.2320/matertrans.I-M2012806.

[4] G. Liu, J. Xiong, Y. Cao, R. Hou, L. Zhi, Z. Xia, W. Liu, X. Liu, C. Glorieux, J.H. Marsh, L. Hou, Visualization of ultrasonic wave field by stroboscopic polarization selective imaging, Opt. Express 28 (18) (2020) 27096–27106, http://dx.doi.org/10.1364/OE.400355.

[5] H. Lu, Y. Cao, H. Zhu, S. Lei, X. Kong, H. Wang, W. Nie, Z. Xi, Dynamic quantitative visualization of transient shear stresses in solids, Opt. Lett. 47 (16) (2022) 4103–4106, http://dx.doi.org/10.1364/OL.461219.

[6] J. Rienitz, Schlieren expreiment 300 years ago, Nature 254 (1975) 293–295, http://dx.doi.org/10.1038/254293a0.

[7] T. Davies, Schlieren photography - short bibliography and review, Opt. Laser Technol. 13 (1) (1981) 37–42, http://dx.doi.org/10.1016/0030-3992(81)90089-X.

[8] J. Rienitz, Optical inhomogeneities: schlieren and shadowgraph methods in the seventeenth and eighteenth centuries, Endeavour 21 (2) (1997) 77–81, http://dx.doi.org/10.1016/S0160-9327(97)01029-6.

[9] T.H. Neighbors, W.G. Mayer, H.J. Ruf, Acousto-optic imaging of focused ultrasound pressure fields, J. Acoust. Soc. Am. 98 (3) (1995) 1751–1756, http://dx.doi.org/10.1121/1.413439.

[10] B. Schneider, K.K. Shung, Quantitative analysis of pulsed ultrasonic beam patterns using a schlieren system, IEEE Trans. Ultrason. Ferroelectr. Freq. Control 43 (6) (1996) 1181–1186, http://dx.doi.org/10.1109/58.542062.

[11] G.S. Settles, Schlieren and Shadowgraph Techniques: Visualizing Phenomena in Transparent Media, Springer Science & Business Media, 2001.

[12] T. Azuma, A. Tomozawa, S. Umemura, Observation of ultrasonic wavefronts by synchronous schlieren imaging, Japan. J. Appl. Phys. 41 (5S) (2002) 3308, http://dx.doi.org/10.1143/JJAP.41.3308.

[13] T. Neumann, H. Ermert, Schlieren visualization of ultrasonic wave fields with high spatial resolution, Ultrasonics 44 (2006) e1561–e1566, http://dx.doi.org/10.1016/j.ultras.2006.05.209, proceedings of Ultrasonics International (UI05) and World Congress on Ultrasonics (WCU).

[14] S.H. Ko, S.G. Ryu, N. Misra, H. Pan, C.P. Grigoropoulos, N. Kladias, E. Panides, G.A. Domoto, Laser induced short plane acoustic wave focusing in water, Appl. Phys. Lett. 91 (5) (2007) 051128, http://dx.doi.org/10.1063/1.2768192.

[15] A. Pulkkinen, J.J. Leskinen, A. Tiihonen, Ultrasound field characterization using synthetic schlieren tomography, J. Acoust. Soc. Am. 141 (6) (2017) 4600–4609, http://dx.doi.org/10.1121/1.4986623.

[16] Z. Xu, H. Chen, X. Yan, M.-L. Qian, Q. Cheng, Three-dimensional reconstruction of nonplanar ultrasound fields using radon transform and the schlieren imaging method, J. Acoust. Soc. Am. 142 (1) (2017) EL82–EL88, http://dx.doi.org/10.1121/1.4994282.

[17] R. Omura, Y. Shimazaki, S. Yoshizawa, S. Umemura, Quantitative measurement of focused ultrasound pressure field using subtraction shadowgraph, Japan. J. Appl. Phys. 50 (7S) (2011) 07HC07, http://dx.doi.org/10.1143/JJAP.50.07HC07.

[18] Y. Shimazaki, S. Harigane, S. Yoshizawa, S. Umemura, Three-dimensional quantitative optical measurement of asymmetrically focused ultrasound pressure field, Japan. J. Appl. Phys. 51 (7S) (2012) 07GF25, http://dx.doi.org/10.1143/JJAP.51.07GF25.

[19] N. Kudo, A simple technique for visualizing ultrasound fields without schlieren optics, Ultrasound Med. Biol. 41 (7) (2015) 2071–2081, http://dx.doi.org/10.1016/j.ultrasmedbio.2015.03.004.

[20] C. Thomsen, H.T. Grahn, H.J. Maris, J. Tauc, Surface generation and detection of phonons by picosecond light pulses, Phys. Rev. B 34 (6) (1986) 4129–4138, http://dx.doi.org/10.1103/PhysRevB.34.4129.

[21] O. Matsuda, M.C. Larciprete, R. Li Voti, O.B. Wright, Fundamentals of picosecond laser ultrasonics, Ultrasonics 56 (2015) 3–20, http://dx.doi.org/10.1016/j.ultras.2014.06.005.

[22] M. Tomoda, O. Matsuda, O.B. Wright, R. Li Voti, Tomographic reconstruction of picosecond acoustic strain propagation, Appl. Phys. Lett. 90 (04) (2007) 041114, http://dx.doi.org/10.1063/1.2432238.

[23] H.N. Lin, R.J. Stoner, H.J. Maris, J. Tauc, Phonon attenuation and velocity measurements in transparent materials by picosecond acoustic interferometry, J. Appl. Phys. 69 (7) (1991) 3816–3822, http://dx.doi.org/10.1063/1.348958.

[24] O.B. Wright, T. Hyoguchi, Ultrafast vibration and laser acoustics in thin transparent films, Opt. Lett. 16 (19) (1991) 1529–1531, http://dx.doi.org/10.1364/OL.16.001529.

[25] H.N. Lin, H.J. Maris, L.B. Freund, K.Y. Lee, H. Luhn, D.P. Kem, Study of vibrational modes of gold nanostructures by picosecond ultrasonics, J. Appl. Phys. 73 (1) (1993) 37–45, http://dx.doi.org/10.1063/1.353859.

[26] O.B. Wright, Laser picosecond acoustics in double-layer transparent films, Opt. Lett. 20 (6) (1995) 632–634, http://dx.doi.org/10.1364/OL.20.000632.

[27] V.E. Gusev, P. Ruello, Advances in applications of time-domain brillouin scattering for nanoscale imaging, Appl. Phys. Rev. 5 (3) (2018) 031101, http://dx.doi.org/10.1063/1.5017241.

[28] B. Audoin, Principles and advances in ultrafast photoacoustics; applications to imaging cell mechanics and to probing cell nanostructure, Photoacoustics 31 (2023) 100496, http://dx.doi.org/10.1016/j.pacs.2023.100496.

[29] M. Tomoda, A. Toda, O. Matsuda, V.E. Gusev, O.B. Wright, Sound velocity mapping from GHz Brillouin oscillations in transparent materials by optical incidence from the side of the sample, Photoacoustics 30 (2023) 100459, http://dx.doi.org/10.1016/j.pacs.2023.100459.

[30] M. Tomoda, A. Kubota, O. Matsuda, Y. Sugawara, O.B. Wright, Time-domain Brillouin imaging of sound velocity and refractive index using automated angle scanning, Photoacoustics 31 (2023) 100486, http://dx.doi.org/10.1016/j.pacs.2023.100486.

[31] B.E. Saleh, M.C. Teich, Fundamentals of Photonics, third ed., John Wiley & Sons, 2019.

[32] C. Glorieux, R. Li Voti, J. Thoen, M. Bertolotti, C. Sibilia, Photothermal depth profiling: analysis of reconstruction errors, Inverse Problems 15 (5) (1999) 1149, http://dx.doi.org/10.1088/0266-5611/15/5/303.

[33] J.F. Power, Inverse problem theory in the optical depth profilometry of thin films, Rev. Sci. Instrum. 73 (12) (2002) 4057–4141, http://dx.doi.org/10.1063/1.1517054.

[34] R. Li Voti, G.L. Leahu, S. Gaetani, C. Sibilia, V. Violante, E. Castagna, M. Bertolotti, Salamone, I. Fratoddi, Light scattering from a rough metal surface: theory and experiment, J. Opt. Soc. Amer. B 26 (8) (2009) 1585–1593, http://dx.doi.org/10.1364/JOSAB.26.001585.

[35] R. Li Voti, G. Leahu, C. Sibilia, R. Matassa, G. Familiari, S. Cerra, T.A. Salamone, I. Fratoddi, Photoacoustics for listening to metal nanoparticle superaggregates, Nanoscale Adv. 3 (16) (2021) 4692–4701, http://dx.doi.org/10.1039/D1NA00333J.

[36] R. Li Voti, G. Leahu, E. Petronijevic, A. Belardini, T. Cesca, C. Scian, G. Mattei, C. Sibilia, Characterization of chirality in diffractive metasurfaces by photothermal deflection technique, Appl. Sci. 12 (3) (2022) 1109, http://dx.doi.org/10.3390/app12031109.

[37] J.-M. Yu, L.-Y. Chen, M.-C. Pan, Y.-F. Hsu, M.-C. Pan, Y.-L. Lin, S.-Y. Sun, C.-C. Chou, In vivo validation of diffuse optical imaging with a dual-direction measuring module of parallel-plate architecture for breast tumor detection, Biomedicines 10 (5) (2022) 1040, http://dx.doi.org/10.3390/biomedicines10051040.

[38] O. Matsuda, O.B. Wright, Reflection and transmission of light in multilayers perturbed by picosecond strain pulse propagation, J. Opt. Soc. Amer. B 19 (12) (2002) 3028–3041, http://dx.doi.org/10.1364/JOSAB.19.003028.

[39] O. Matsuda, O.B. Wright, Laser picosecond acoustics with oblique probe light incidence, Rev. Sci. Instrum. 74 (1) (2003) 895–897, http://dx.doi.org/10.1063/1.1519679.

[40] G. Tas, H.J. Maris, Electron diffusion in metals studied by picosecond ultrasonics, Phys. Rev. B 49 (21) (1994) 15046–15054, http://dx.doi.org/10.1103/PhysRevB.49.15046.
[41] S. Kashiwada, O. Matsuda, J.J. Baumberg, R. Li Voti, O.B. Wright, In situ monitoring of the growth of ice films by laser picosecond acoustics, J. Appl. Phys. 100 (7) (2006) 073506, http://dx.doi.org/10.1063/1.2353125.
[42] Data Sheet of N-BK7 517642.251, https://www.schott.com/shop/advanced-optics/en/Optical-Glass/N-BK7/c/glass-N-BK7.
[43] E.D. Palik (Ed.), Handbook of Optical Constants of Solids, Academic Press, Boston, 1998.
[44] O.B. Wright, Ultrafast nonequilibrium stress generation in gold and silver, Phys. Rev. B 49 (14) (1994) 9985–9988.
[45] D.R. Lide (Ed.), CRC Handbook of Chemistry and Physics, eightyfifth ed., CRC Press, Boca Raton, Fla, 2004.
[46] C.F. Quate, A. Atalar, H. Wickramasinghe, Acoustic microscopy with mechanical scanning—a review, Proc. IEEE 67 (8) (1979) 1092–1114, http://dx.doi.org/10.1109/PROC.1979.11406.
[47] R.W. Dixon, Photoelastic properties of selected materials and their relevance for applications to acoustic light modulators and scanners, J. Appl. Phys. 38 (13) (1967) 5149–5153, http://dx.doi.org/10.1063/1.1709293.
[48] S. Sandeep, S. Raetz, N. Chigarev, N. Pajusco, T. Thréard, M. Edely, A. Bulou, A. Zerr, V.E. Gusev, Time-domain Brillouin scattering for evaluation of materials interface inclination: Application to photoacoustic imaging of crystal destruction upon non-hydrostatic compression, Photoacoustics 33 (2023) 100547, http://dx.doi.org/10.1016/j.pacs.2023.100547.

Motonobu Tomoda received his Ph.D. degree in engineering at Hokkaido University, Sapporo, Hokkaido, Japan, in 2008. Since 2022, he has been working as an instructor (until 2007) and an assistant professor (from 2007) in the Faculty of Engineering, Hokkaido University. He specializes in picosecond laser ultrasonics in nanostructures, local probing techniques involving ultrasonics and optics, surface acoustic wave imaging, phononic crystals, and acoustic/mechanical metamaterials.

Hiroyuki Matsuo received his B.A. degree in engineering in 2010 and his master's degree in 2012 from Hokkaido University, Sapporo, Hokkaido, Japan. His research interests include laser picosecond ultrasonics.

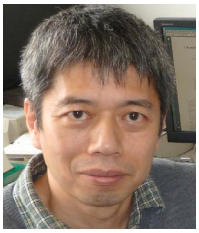

Osamu Matsuda received his Ph.D. degree in physics at Osaka University, Japan in 1991. He is currently a professor at Hokkaido University, Japan. His research interests include ultrafast spectroscopy, picosecond laser ultrasonics, acoustic wave imaging, phononic crystals, and phononic metamaterials.

Prof. Roberto Li Voti is the Head of the Photothermal and Photoacoustic Laboratory at the Sapienza University of Rome, Italy. He is expert in photothermal deflection techniques, photothermal and photoacoustic spectroscopy, photothermal radiometry and infrared thermography for the nondestructive and quality testing of materials. He also has expertise in thermal diffusivity, optical and thermal depth profiling, detection of buried layers, and in the nondestructive testing of photovoltaic, nanophotonic, nanophononic and nanoplasmonic materials, in trace gas analysis, and in bioactive molecule detection.

Oliver B. Wright has been a Professor at Hokkaido University, Japan since 1996 and a Guest Professor at Osaka University, Japan since 2022. He received his BA in physics at the University of Oxford and his Ph.D. in physics from the University of Cambridge. His current research interests include picosecond laser ultrasonics, acoustic wave imaging, and acoustic metamaterials.